Tablet boudinage of an anhydrite layer in rock-salt matrix: Results from thermomechanical experiments

J. Zulauf [a,*], G. Zulauf [a], J. Hammer [b], F. Zanella [c]

[a] Institut für Geowissenschaften, Universität Frankfurt a.M., Altenhöferallee 1, D-60438 Frankfurt a.M., Germany
[b] Bundesanstalt für Geowissenschaften und Rohstoffe, Stilleweg 2, D-30655 Hannover, Germany
[c] Institut für Neuroradiologie, Universität Frankfurt a.M., Theodor-Stern-Kai 7, 60596 Frankfurt a.M., Germany

ARTICLE INFO

ABSTRACT

A single competent layer of anhydrite, embedded in a matrix of incompetent rock salt, was deformed in a flattening type of bulk deformation at temperature, $T = 345\ °C$, strain rate, $\dot{e} = 10^{-7}\ s^{-1}$, to a maximum finite strain, $e_Z = -30\%$. As the anhydrite layer was oriented perpendicular to the main shortening direction, Z, the layer underwent equal layer-parallel extension in all directions resulting in tablet-shaped boudins. Boudinage results from tensile fracture of anhydrite. The rock-salt matrix, on the other hand, behaved viscously. Crystal plastic deformation of halite was accommodated by slip on {110}<110> which led to formation and rotation of subgrains and a 001-maximum parallel to the principal shortening axis, Z. An axisymmetric texture of halite, however, is present only in high-strain domains at the contact to the anhydrite layer where the differential stress, obtained from subgrain size of halite, reaches maximum values of ca. 6 MPa. Subgrains remote from the anhydrite layer yielded 2–3 MPa, which is consistent with the flow stress recorded by the load cell of the machine.

The non-isometric shape of the tablet boudins in plan-view is indicated by the ratio between long and short axis ($R = 1.2$–1.9), and can be explained by the interaction of concentric and radial tensile fractures. Both the mean diameter of the tablet boudins in plan-view, W_a, and the number of boudins, N, show a linear relation to the layer thickness. Progressive finite strain results in a higher number and a smaller mean diameter of the boudins. The thickness of the boudins, H_f, is almost the same like the initial layer thickness, H_i, while the aspect ratio ($W_d = W_a/H_f$) decreases with finite strain. The mean W_d values obtained from all runs are ranging from ca. 0.8 to ca. 1.5. This range is much lower than the aspect ratio of boudins in viscous or brittle/viscous layers, but is similar to the aspect ratio expected from fracture-saturation models. The aspect ratio of the tablet-shaped anhydrite boudins is further consistent with aspect ratios published so far for tensile-fracture boudins which developed in a plane or constrictional type of bulk deformation.

© 2011 Elsevier Ltd. All rights reserved.

1. Introduction

Deformation structures in salt rocks can be studied more readily than those of other crystalline rocks, as salt rocks were deposited horizontally and their present shape and attitude has been revealed in three dimensions by mining, drilling and 3D seismic studies (e.g. Talbot et al., 1982; Jackson and Talbot, 1987; Jackson, 1995; Hudec and Jackson, 2007; Bornemann et al., 2008; Van Gent et al., 2011). A further advantage of salt rocks is the fact that their deformation can be studied experimentally far more readily than the deformation of silicate rocks (e.g. Guillopé and Poirier, 1979; Skrotzki and Welch, 1983; Gairola and Kern, 1984; Spiers et al., 1990; Carter et al., 1993; Franssen, 1994; Ter Heege et al., 2005; Zulauf et al., 2009).

The finite strain in deformed salt rocks is frequently inhomogeneous. There are different rock types, which do not deform with equal readiness. Among dry salt and associated sediments the viscosity should decrease in the following order: dolomite > marl > 'dry' saliferous clay > anhydrite > kieseritic rocks > halite > sylvite > carnallite > bischofite (Borchert and Muir, 1964, p. 248). In cases where two or more of these rocks are interbedded as layers, folding or boudinage may affect the more competent of the two. Of particular importance is rock salt, which occurs in the middle of the above viscosity sequence. We are using the term 'rock salt' for all rocks composed of mostly halite (Hudec and Jackson, 2007). Rock salt is mechanically weak and flows at

low stresses (<ca. 5 MPa), even at low temperatures and at geologically high strain rates (Schoenherr et al., 2007; Urai and Spiers, 2007). If rock salt is interbedded with anhydrite, the latter is forming the stiff competent layer, whereas rock salt is forming the weak incompetent matrix (e.g. Bornemann et al., 2008; Zulauf et al., 2009). On the other hand, rock salt may form a competent layer if surrounded by weaker incompetent carnallite matrix (e.g. Siemeister, 1969).

In the present paper we focus on the development of non-cylincrical anhydrite boudins, which are embedded in weaker rock salt matrix. Composite samples consisting of both rock types have been deformed experimentally at elevated temperature in a flattening type of bulk deformation, with the anhydrite layer oriented perpendicular to the main shortening direction, Z. It is commonly assumed that under these oblate conditions chocolate tablet boudinage should develop (e.g. Weijermars, 1997, p. 250). Field studies, on the other hand, suggest that chocolate-tablet boudinage requires polyphase deformation (e.g. Reber et al., 2010; Zulauf et al., 2011b). If the oblate strain arises *during a single deformation*, the necks between boudins will generally be rather irregular and the boudins will be polygonal and tablet shaped in plan-view. This particular structure has been confirmed experimentally by Ghosh (1988) and by Zulauf et al. (2011a) using rock analogues. Tablet-shaped boudins did also develop in the present study by tensile failure of the anhydrite layer. Their 3D-geometry and microfabrics will be described in the following sections. It will be shown that the mode of layer dissection (brittle tensile failure vs. viscous necking) has a significant impact on the size and geometry of tablet boudins, which result from layer-parallel extension in a flattening type of bulk deformation.

2. Experimental procedure and analytical techniques

2.1. Material and models

We deformed composite samples consisting of rock salt as matrix (almost pure halite of the Asse of northern Germany, 800 m level, Speisesalz Na2SP) and natural anhydrite as embedded layer (anhydrite of the Gorleben deep borehole 1004). All samples were delivered by BGR Hannover. For details on the composition of the anhydrite and rock salt as well as the preparation of composite rock salt/anhydrite samples, see Zulauf et al. (2009).

The initial dimension of the three-layer models (rock salt + anhydrite layer) was $57 \times 60 \times 60$ mm. During bulk pure flattening of the samples, the anhydrite layer was oriented perpendicular to the shortening axis, Z, of the finite strain ellipsoid. Deformation conditions during each run were as follows: $T = 345\ °C$, $\dot{e} = 1 \times 10^{-7}\ s^{-1}$–$5 \times 10^{-7}\ s^{-1}$, and $e_Z = -30\%$. Under these conditions Asse rock salt should deform by viscous creep, which is accommodated by subgrain rotation, whereas Gorleben anhydrite deforms under brittle-viscous conditions (see Zulauf et al., 2011a, and references therein). The viscosity of the non-linear viscous rock salt is ca. 5×10^{12} Pa s (at the strain rate used in the experiments, see below). To investigate the impact of the initial thickness of the anhydrite layer, H_i, the latter was set at 1.0, 1.5, 2.0, and 2.5 mm. The uncertainty of the layer thickness is ± 0.1 mm. As we are dealing with fracture boudinage of the anhydrite layer (see below), the modeling results of Bai and Pollard (1999) should be considered concerning the dimension of stiff layer and weak matrix. These results suggest that if the adjacent incompetent layers are thicker than 1.5 times of the fractured layer, the multilayer can be treated approximately as a system with infinitely thick top and bottom layers in terms of spacing at fracture saturation.

A second series of experiments was carried out incrementally to investigate the impact of finite strain on the deformation geometry of the anhydrite layer, the latter with initial thicknesses of 2.0 ± 0.1 mm. The deformation was stopped after strain increments of $e_Z = -10\%$ until the final strain of -30% was obtained. The strain rate was set at $1 \times 10^{-7}\ s^{-1}$. After having imposed the respective incremental strain, deformation was stopped and the sample cooled down until room temperature was obtained. Subsequently the sample was removed from the apparatus and analyzed using computer tomography (CT) which is described below.

As the present experiments were carried out to model deformation of rock salt and anhydrite in nature, the models must be properly scaled. The *scaling procedure* should include geometrical, kinematical and dynamical similarity (e.g. Hubbert, 1937; Ramberg, 1981). As each type of modeling is restricted to small-scale structures at relatively low strain rates, the influence of body forces (inertial and gravity) can be neglected. Geometrical similarity is given as the model is a reduced or enlarged geometric replica of the original rock. Kinematical similarity is maintained as corresponding particles are found at corresponding places at corresponding times. Compared with naturally deformed rocks, there is only a difference in strain rate which has to be considered. Rock salt is unusually soft and the range of natural strain rates 10^{-16}–$10^{-8}\ s^{-1}$ it exhibits is probably close to the extreme in natural solid-state rock flow (Jackson and Talbot, 1986). The high strain rate in the experiments implies higher viscous stress in the rock salt compared to natural conditions, whereas the elastic stress in the anhydrite depends on the strain, which is the same in experiment and nature. Thus, dynamic similarity is given if strain rates in nature are similar high as the experimental strain rates. In such cases the ratio between viscous stress in rock salt and elastic stress in anhydrite is almost the same in nature and experiment.

Natural examples which are equivalent to the models of the present studies could be: (1) brittle dolomite layer embedded in viscous calcite matrix deforming in the lower greenschist facies; (2) amphibolite or calc-silicate layer embedded in gneiss matrix deforming in the upper greenschist facies. Last but not least the halite and anhydrite used in the present study are natural rocks. Given that in particular cases the strain rate in nature is similar to the strain rate used in the present experiments (ca. $10^{-7}\ s^{-1}$), the model could be directly related to the deformation of halite and anhydrite in nature. The only problem will be the lack in confining and pore pressure.

2.2. Deformation apparatus

Deformation of the composite halite-anhydrite samples was performed using a thermomechanical deformation rig described in detail by Zulauf et al. (2009). The deformation rig consists of a stable frame made of steel in which four aluminium plates have been orthogonally assembled. The sample is sandwiched between the four plates. One of the plates is immobile, while fixed to the frame. The other plates are moving along sledges. They are driven by two separate three-phase stepping motors via a gear.

To increase the temperature of the plates, the latter are subdivided into 3 zones, each of which contains 4 heating cartridges. The temperature of each plate is measured by 7 thermocouples. At pre-scribed time intervals the temperature values are recorded by the control unit and adjusted to the target value. The heating cartridges support a maximum deformation temperature of 375 °C with an uncertainty of less than 0.1 °C.

Measurements of in-situ stresses allow constraining in-situ viscosities in the direction of the principal strain axes. There are two single-point load cells, each fixed at one plate, and linked with

the control unit to determine the horizontal and vertical stress during deformation.

During an experimental run, the temperature, stress and strain data are recorded for pre-scribed time intervals (24 s in the present case) and stored in EXCEL format. Deformation of halite/anhydrite has to be performed at slow strain rates (10^{-7} s^{-1}) resulting in a deformation period of >3 weeks for each experiment if finite strain is moderate.

When putting the halite-anhydrite sample into the sample space of the deformation apparatus, caution is needed. While the sample is heated up from room temperature to $T = 345$ °C, halite will show significant thermal expansion (0.78 mm). Thus, sufficient space is needed between the sample and the moving plates before the heating is switched on. To be sure that during deformation the temperature of the sample is the same as the temperature of the plates, the motors of the machine were switched on ca. 12 h after the pre-scribed temperature (345 °C) was reached by the plates. Because of the large difference in thermal expansion between the halite matrix and the anhydrite layer, the composite sample was heated slowly (20 °C h^{-1}). If the prescribed finite strain was reached, the motors were stopped and the temperature of the sample was slowly reduced (ca. 20 °C h^{-1}) until room temperature was obtained.

2.3. Geometric analysis of deformation structures

The geometry of ribbon-like cylindrical boudins can be conveniently analysed in two dimensions, i.e. in sections cut perpendicular to the long axis of the boudins. Noncylindrical boudins, like those of the present study, however, cannot be analyzed by these simple techniques. In the present case of rock salt/anhydrite interbeddings, we used the advantage of the density contrast between both rock types which allows computer tomography (CT) to be applied for analyzing the deformation structures in 3D. All of the deformed samples have been investigated by CT and conventional sections, the latter cut parallel to the principal shortening axis, Z (for details, see Zulauf et al., 2003, 2009). As a sufficient contrast in density is given between the anhydrite layer (2.9 g cm^{-3}) and the rock salt matrix (2.3 g cm^{-3}), there is no problem to visualize the deformation structures of the anhydrite layer using CT. In cases where the thickness of the competent anhydrite layer was >1 mm, CT-studies were performed at the clinic of Frankfurt University in the Neuroradiologie Department using a multislice spiral CT-scanner (*Phillips CT Brilliance* with 6 lines). Conditions for analyzing the samples were as follows: slice thickness = 0.8 mm, spacing = 0.6 mm, standard voxel resolution.

In the case where the anhydrite layer was only 1 mm thick, CT-studies were performed using the high-resolution Nanofocus Computertomograph *nanotom 180* at the Geoscience Department of Frankfurt University. Conditions for analyzing the samples were as follows: acceleration voltage = 150 kV, voxel resolution = 60 μm.

Geometrical parameters of folds and boudins have been determined from CT images using the software *Smooth*, which supports production, visualisation, and analyses of DICOM volumetric data. Apart from central projection, there is a possibility to present the 3D models in parallel projection. The latter type is used when measuring geometric data (length, angle, area) on the screen. To constrain the geometry of the deformed stiff layer, only the latter was shown in the CT images, whereas the matrix was removed.

The distribution of boudin necks is analyzed in plan-views (*XY*-sections) and shown in rose diagrams. All geometric parameters like length, angle etc. were determined using image analysis software. During the counting procedure only those boudins were considered, which are entirely or almost entirely separated from the rest of the layer.

The outlines of the boudins were digitized in plan-views. Subsequently, the area as well as the direction and length of the long and short axes of the boudins were determined using image analysis software. From the boudin area in plan-view the mean boudin diameter, W_a, was obtained by calculating the diameter of a circle equivalent in area to that of the boudin. The ratio between long and short axis, R, describes the shape anisotropy of the boudins in plan-view.

The fracture spacing to layer thickness ratio, referred to as aspect ratio, W_d, is calculated by dividing the mean diameter of the boudin, W_a, through the finite layer thickness, H_f. Because of strong boundary effects (see below), geometrical parameters have not been determined from necks and boudins of the marginal parts of the deformed samples.

2.4. Microfabric studies

Thin and thick sections were prepared from undeformed halite and anhydrite samples and from sections of deformed samples which are oriented parallel to the Z-axis of the finite strain ellipsoid. To reveal the grain and subgrain boundaries in halite, we used the method described by Urai et al. (1987). After polishing the sections with colloidal diamond dispersed in oil (0.25 and 1 μm), the sections were lightly etched for 30 s using a 95% saturated NaCl solution containing 0.8 wt% FeCl$_3$ x 6H$_2$O. Subsequently the etchant was removed from the surface using a powerful jet of n-hexane, and the section was dried in a stream of warm air.

Grain boundaries and subgrains in halite could be found in etched samples using transmitted or reflected light. The size of the subgrains was required for piezometry. To determine the average diameter of subgrains, D, from etched sections, the outlines of the subgrains were digitized, and subsequently the area of the grains was determined using image analysis software. From the grain area the average grain diameter was obtained by calculating the diameter of a circle equivalent in area to that of the subgrain.

2.5. Electron backscatter diffraction (EBSD) analyses

The application of electron backscatter diffraction to the study of halite microfabrics provides information about a lattice preferred orientation in rock salt (e.g. Pennock et al., 2005; Bestmann et al., 2005; Schléder and Urai, 2007; Zulauf et al., 2010). This technique was applied to polished sections cut perpendicular to the Z-direction using an in-house equipment. The samples were coated with carbon up to a thickness of about 4 nm to reduce charging effects. Crystallographic orientation data were obtained from EBSD patterns using a JEOL JSM-6490, typically operating with an acceleration voltage of 15 keV and beam current of 8 nA. The EBSD patterns were indexed with the CHANNEL 5 software (HKL Technologies) using the file for halite consisting of 46 lattice planes. Multiple beam maps were used to map the specimen. For an individual map, data points were collected on a rectangular area at a fixed step size of 13 μm by moving the sample and keeping the beam stationary. After the mapping, the individual maps were stitched together using the CHANNEL 5 software. The texture is displayed in form of inverse pole figures which are plotted as contour maps over the standard triangle for the cubic symmetry. A contour of unity corresponds to a randomly orientated sample.

3. Results

3.1. Impact of layer thickness on geometry of boudins

One set of experiments was carried out to reveal the impact of the initial layer thickness, H_i, on the deformation geometry. Before
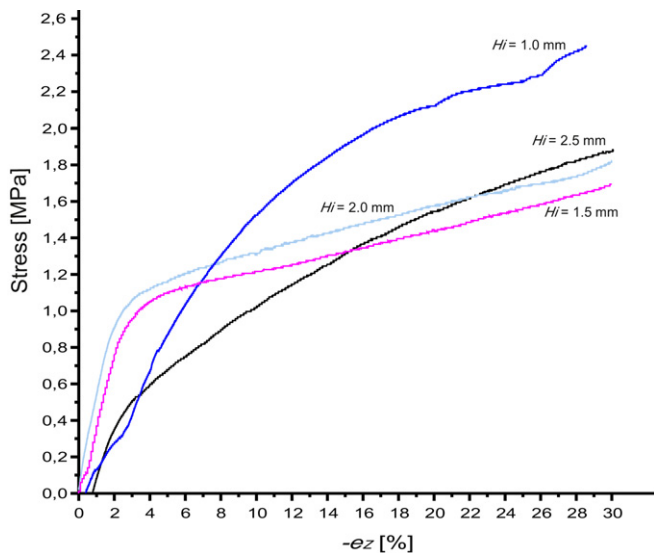
Fig. 1. Stress vs. strain diagram of four different runs under bulk pure flattening where the initial thickness of anhydrite, H_i, was changed.

describing the geometry of the deformed anhydrite layer, we will briefly focus on the stress vs. strain plots. Note that the stress was monitored continuously during each experiment along the Z-axis, meaning that the single-point load cell was placed on top of the halite matrix and the stress was measured in a direction perpendicular to the stiff anhydrite layer.

A strikingly similar flow curve is given for the runs with $H_i = 1.5$ and 2.0 mm. There is a distinct change in the direction of the flow curves at $e_Z = $ ca. 3%, where the elastic stage is succeeded by viscous creep, the latter with moderate strain hardening (Fig. 1). Maximum stresses along the Z-axis, recorded at 30% strain, were 1.8 and 1.7 MPa resulting in a viscosity of ca. 2.5×10^{12} Pa s at the experimental strain rate of $\dot{e} = 10^{-7}$ s^{-1}. The flow curve for the sample with layer thickness $H_i = 2.5$ mm shows a similar maximum stress like the samples mentioned above, but the change from elastic to viscous behavior is less distinct. The same indistinct change from elastic to viscous behavior holds for the sample where $H_i = 1.0$ mm. However, in this case the maximum stress at 30% strain was 2.5 MPa which implies a viscosity of 3.5×10^{12} Pa s at the experimental strain rate of $\dot{e} = 10^{-7}$ s^{-1}.

The deformed samples show strikingly different patterns of necks and boudins with increasing layer thickness. A section through a deformed sample, cut perpendicular to the layer, is shown in Fig. 2a. If the layer was thick, the viscous halite has only partly filled the necks and the central part of the neck is still open (Fig. 2b). In cases where the layer was thin, however, the viscous halite was able to entirely fill the necks between the anhydrite boudins. The intensity of boudinage decreases from the centre to the margin of the sample. In the marginal parts the boudins are large and nearly rectangular in shape (Fig. 3). In the central part of the sample the boudins are small and polygonal. The ends of the boudins do not show evidence for pinching out. The dissection plane is in most cases undulated or serrated. The thickness of the deformed layers, H_f, is almost the same like the initial layer thickness, H_i (Fig. 4).

The change in geometric pattern with layer thickness is particularly well documented in plan-views of CT images where the anhydrite boudins occur as isolated polygonal tablets (Fig. 5a–d). There is a clear pattern of radial necks, particularly in the marginal parts of the samples. Some of the layers show additional concentric necks, which are particularly well developed in the case where $H_i = 1.5$ mm (Fig. 5c). As the grade of boudinage decreases towards the margins of the sample, the size of the boudins increases from centre to the margin. The direction of necks does not show a significant preferred orientation in plan-views as is shown by the rose diagrams (Fig. 5a–d).

With increasing layer thickness, H_i, the mean diameter of the boudins in plan-views, W_a, increases almost linearly from ca. 1.5 to ca. 3.0 mm (Fig. 6a). This relation is given by equation:

$$W_a = 0.3 \pm 0.9 + 1.1 \pm 0.6 * H_i \qquad (1)$$

The aspect ratio of the boudins ($W_d = W_a/H_f$) does not significantly change with layer thickness. The W_d-values are ranging from 0.8 to 1.8 when considering the error bars (Fig. 6b). The number of boudins, N, decreases almost linearly from ca. 240 to 70 (Fig. 6c) according to the following equation:

$$N = 354 \pm 20 + -111 \pm 11 * H_i \qquad (2)$$

Similar to the aspect ratio, the ratio between long and short boudin axis in plan-view, R, is hardly controlled by the initial layer thickness. The R-values obtained are ranging from 1.2 to 1.8 when considering the error bars (Fig. 6d).

3.2. Impact of finite strain on deformation geometry

The stress vs. strain curves of the incremental study are depicted in Fig. 7. The first strain increment ($e_Z = 0$ to -10%) shows a change from elastic to viscous behavior at $e_Z = $ ca. -3% and $\sigma_1 - \sigma_3 = $ ca.
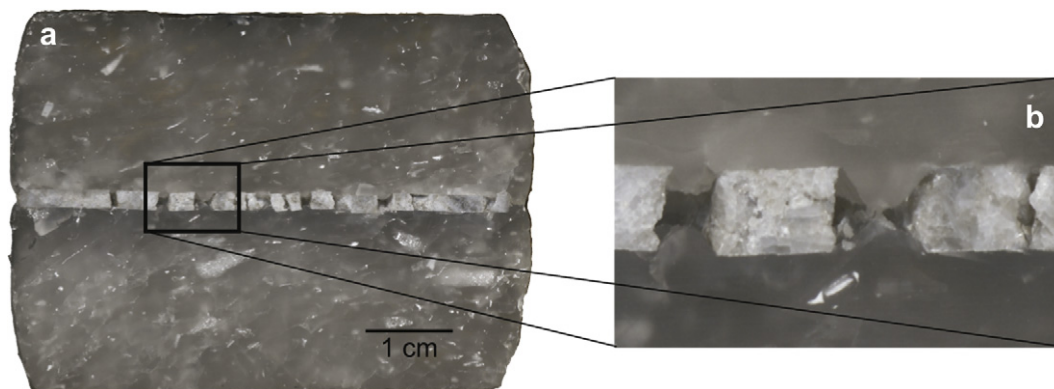

Fig. 2. (a) Section of deformed sample cut parallel to the Z-axis and perpendicular to anhydrite layer. Initial thickness, Hi, of anhydrite layer = 2.5 mm. Note fracture boudinage of anhydrite layer inside viscous halite matrix. (b) Close-up view of area marked by black frame in (a). Necks between the anhydrite boudins are not entirely filled with viscous halite because of the large layer thickness.
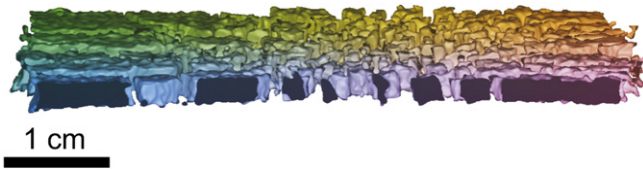
Fig. 3. Computertomographic (CT) image with section through deformed anhydrite layer. Initial layer thickness, H_i, is 2.0 mm. View is slightly oblique to the deformed layer. Scale bar at lower left is valid only for the section area of the boudins of the layer shown in black.

Fig. 4. Initial layer thickness (H_i) versus finite layer thickness (H_f).

1 MPa. The viscous flow shows considerable strain hardening. Due to this strain hardening the plastic yielding during the second increment ($e_Z = -10$ to -20%) is attained at a differential stress of ca. 1.4 MPa, which is considerably higher than the yield stress of the first increment. However, compared to the first strain increment, the degree of strain hardening is less strong during the second increment as is shown by the stress-strain curve. During the third strain increment ($e_Z = -20$ to -30%) the stress-strain conditions are similar to those of the second increment.

Geometrical analyses of the deformed samples suggest that incipient boudinage occurred already at 10% finite strain (Fig. 8a). The central part of this sample shows a circular domain, ca. 3 cm in diameter, which is affected by many small-scale necks. In this part most of the anhydrite boudins are not entirely separated from the remaining layer. In the centre of the circular necked domain there is one boudin which is almost circular in shape and ca. 3 mm in diameter. This tablet-shaped boudin is surrounded by a concentric neck from which several radial necks are arising. The margin of the sample outside the circular necked domain is free from small-scale necks but shows a pattern of larger radial necks which are largely straight. The width of these necks increases towards the rim of the layer.

At 20% finite strain a large number of boudins has developed (Fig. 8b). Most of these boudins are entirely separated from the remaining layer. This holds for the central part of the sample, which is similar in shape and size like the circular necked domain of the sample with 10% strain described above. The shape of the boudins is polygonal. The width of the radial necks in the marginal parts of the layer has increased and the number of radial necks is also larger compared to the previous state of strain. This trend is still more obvious at 30% finite strain (Fig. 8c). The direction of necks does not show a significant preferred orientation in plan-views as is shown by the rose diagrams (Fig. 8a–c).

The size of the boudins is strongly controlled by the finite strain. The mean diameter of boudins in plan-views decreases linearly with finite strain from ca. 3 to ca. 2 mm (Fig. 9a). This relation can be described by the equation:

$$W_a = 3.5 \pm 0.9 + -0.05 \pm 0.04 * e_Z \tag{3}$$

The aspect ratio of the boudins ($W_d = W_a/H_f$) shows the same trend and decreases from ca. 1.2 to 0.8 (Fig. 9b). The number of boudins, N, increases from ca. 6 to ca. 150 (Fig. 9c). The ratio between long and short boudin axis in plan-view, R, is not controlled by the finite strain. The R-values obtained are ranging from 1.2 to 1.9 when considering the error bars (Fig. 9d).

3.3. Microfabrics of anhydrite

There are two different types of anhydrite in the samples: (1) the primary tiny inclusions of anhydrite inside Asse rock salt, and (2) the Gorleben anhydrite forming the competent layer between the matrix of Asse rock salt. I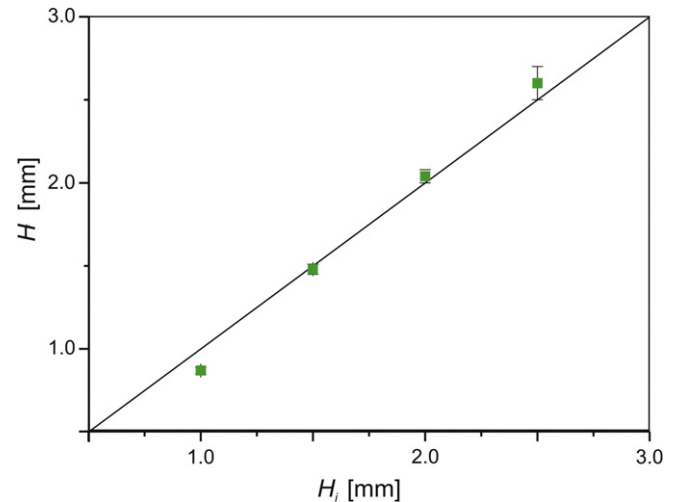nclusions of anhydrite with grain size up to 4 mm are present within the halite grains and along halite grain boundaries. In the original samples these anhydrite inclusions do not show a shape-preferred orientation and are largely free from deformation fabrics.

The grain size of anhydrite of the initial Gorleben samples varies considerably from <100 μm to 10 mm. Most of these grains show primary growth fabrics and a dirty habitus, the latter resulting from numerous fluid inclusions and opaque phases. Rosette shaped aggregates of anhydrite are frequently present on almost all scales. The anhydrite rosettes are partly truncated by highly lobate seams which are rich in fluid inclusions and opaque phases. These seams are common in Zechstein anhydrite and reflect localized dissolution-reprecipitation creep (Bäuerle, 1998; Bornemann et al., 2008). Local, but weak crystal plastic strain is documented by rare twinning on the {101} planes and by weak bending of long-prismatic crystals.

The primary anhydrite inclusions inside Asse halite matrix were reoriented due to flattening strain with the long axis being aligned subparallel to the XY-plane. As these inclusions were flowing in much weaker halite, they do not show noticeable internal crystal plastic strain.

The principal deformation fabric of experimentally deformed layers of Gorleben anhydrite is fracturing along the cleavage planes, which was also described by Zulauf et al. (2009, 2010) from constrictional experiments carried out under similar conditions. Cataclastic deformation of anhydrite in the neck domains results in strong grain size reduction with porphyroclasts being embedded in the viscous halite matrix. Most of the boudins contain microfractures.

Crystal plastic strain is recorded by undulatory extinction, deformation twins, bending of long-prismatic crystals, and serrated grain boundaries, the latter reflecting strain-induced grain-boundary migration which results in smaller recrystallized grains. In contrast to the host grains, these new grains are largely free from impurities. Most of the recrystallized grains are almost isometric with diameters ranging from 20 to 70 μm. Some of them display undulatory extinction.

3.4. Microfabrics of halite

For the present studies we selected samples of Asse halite, which are only weakly deformed and largely free from a grain-shape fabric. The size of the halite grains is 4.2 ± 2 mm. The
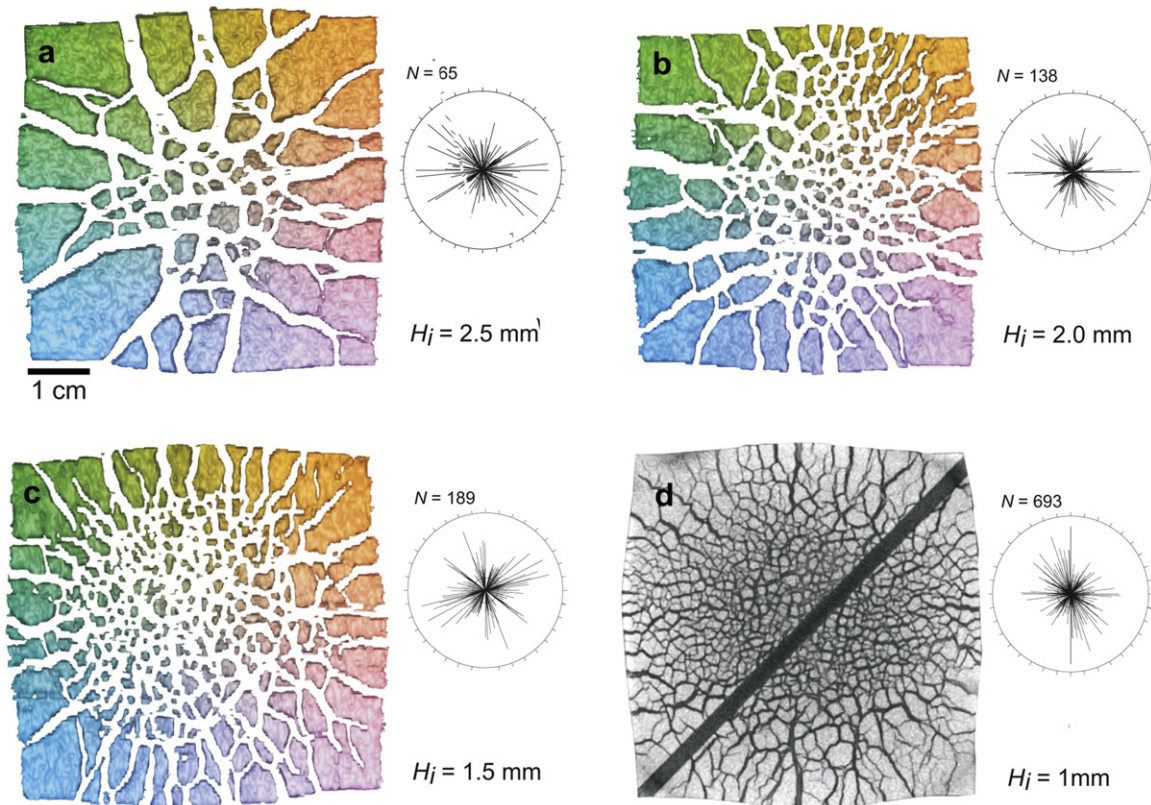
Fig. 5. Computertomographic (CT) images (plan-view) of deformed anhydrite layer showing the impact of increasing layer thickness on the geometry and number of boudins. View is perpendicular to the layer and parallel to the main shortening direction, *Z*, respectively. Initial layer thickness, H_i, is 2.5 mm (a), 2.0 mm (b), 1.5 mm (c), 1.0 mm (d). Note that (a)–(c) is based on analyses with a medical computertomograph, whereas (d) is based on micro-computertomography. The diagonal section through sample (d) results from cutting before CT analysis. Rose diagrams show the distribution of necks in the deformed sample. N is number of measurements.

grains are almost free from crystal plastic strain as is revealed by etched and irradiated samples. Grain boundaries are either straight or weakly lobate. Subgrains are rare and largely restricted to the surroundings of rigid anhydrite inclusions. The size of these subgrains ranges from ca. 60 to ca. 80 μm.

A striking feature of all of the initial halite samples is the presence of grain-boundary fluid inclusions which have already been described in detail from other Asse samples (Urai et al., 1987; Zulauf et al., 2010). These fluid inclusions are regularly distributed along the grain boundaries in most of the initial samples. Investigations using fluorescence microscopy and Raman spectroscopy revealed that most of the fluid inclusions consist of NaCl brine and organic matter, the latter including methane (Zulauf et al., 2010).

The deformed samples show a strong oblate grain-shape fabric of halite grains which is particularly strong at the contact to the anhydrite layer. In contrast to the initial samples the halite grains are strongly elongated due to crystal plastic deformation.

In etched samples cut parallel to the *Z*-axis crystal plastic strain is frequently recorded by subgrains with irregular, polygonal boundaries (thin dark lines inside the grains depicted in Fig. 10a). In some cases a rectangular grid of discrete dark lines is present with the *Z*-axis forming the angle bisector (Fig. 10b). EBSD analyses revealed that these dark lines reflect both subgrain boundaries and newly formed high-angle grain boundaries which are forming a chessboard pattern. A similar type of chessboard patterns of subgrains have been observed in halite which was deformed under similar conditions but under bulk constriction (Zulauf et al., 2010). Away from the anhydrite layer, the subgrain size varies from grain to grain (50−130 μm, Table 1). The subgrain

size increases significantly towards the rigid anhydrite layer (Fig. 10c). At the direct contact to the layer the size is reduced to 20−60 μm (Table 1). A similar pattern of subgrains is present inside the halite, which intruded into the open necks between the anhydrite boudins. The inner part of this invading halite is characterized by polygonal subgrains which have a normal size like those of the other grains, whereas the margin towards the open space of the neck domain is showing subgrains which have a very small size similar to the halite situated at the direct contact to the anhydrite layer (Fig. 10c).

EBSD analyses of deformed halite grains, situated at the contact to the anhydrite layer, revealed an axisymmetric texture with a striking 001-maximum parallel to the *Z*-axis as is shown in inverse pole figures (Fig. 11a). As pure flattening strain is axisymmetric, the inverse pole figures describe the texture completely. Away from the halite layer, most of the grains do not show an axisymmetric texture. EBSD analyses have further shown that some of the subgrains did rotate resulting in high-angle grain boundaries which are separating new recrystallized grains. Statistical data on the misorientation-angle distribution of two different primary grains are shown in Fig. 12. Most of the grains are subgrains with misorientation angles <5°. The misorientation angle of most of the recrystallized grains varies from 30 to 60°. Misorientation angles between 10 and 30° are less frequent or absent.

3.5. Piezometry using subgrain size of halite

Experimental deformation of various minerals and rocks revealed a strong correlation between the steady state subgrain size, *D*, and flow stress (e.g. Twiss, 1977). Based on calibrations
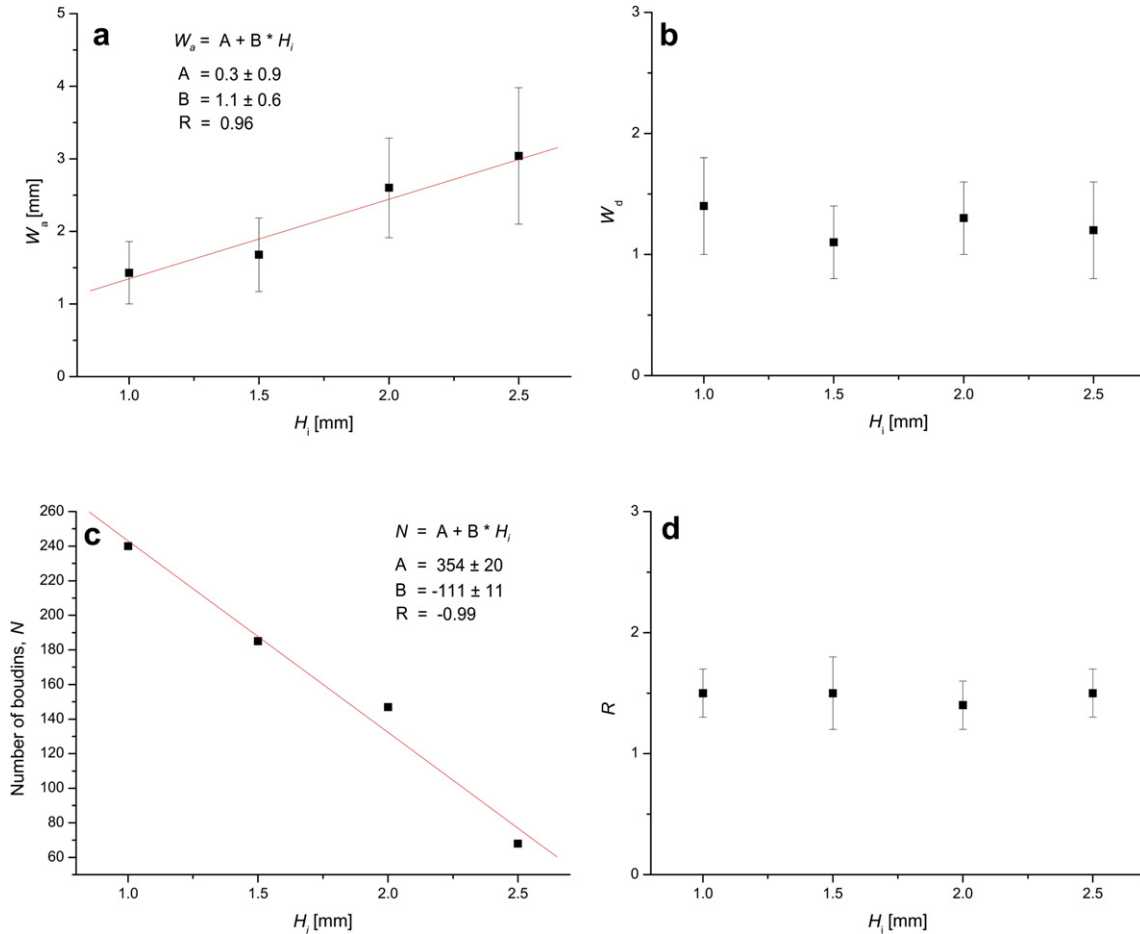
Fig. 6. Geometric data of competent anhydrite layer embedded in viscous matrix of rock salt deformed under bulk pure flattening conditions with the layer perpendicular to Z. Geometric parameters are plotted vs. initial layer thickness, H_i. N = number of boudins, R = ratio between long and short axis of boudin in plan-view; W_a = mean diameter of boudins in plan-views, $W_d = W_a/H_f$ = aspect ratio of boudins. Deformation temperature, $T = 345$ °C; finite strain, $e_Z = -30\%$; strain rate, $\dot{e} = .1 \times 10^{-7}$ s^{-1}. Data shown have been obtained by Computer Tomography (CT) and by analysis of common sections cut parallel to Z and perpendicular to the layer.

obtained by Carter et al. (1993) and Franssen (1993) using experimentally deformed rock salt, this relationship can be written as

$$D[\mu m] = 215\sigma'^{-1.15}[MPa] \qquad (4)$$

(Schléder and Urai, 2005). Equation (4) has been used for estimating the stress, σ', in deformed Asse halite that was compared with the actual stress values, σ, recorded by the single-point load cells during each experimental run. The number of subgrains considered in one sample ranges from 70 to 200. The following conditions should be met when using this method of piezometry: (i) the size of subgrains should not be influenced by secondary phases like anhydrite; (ii) the subgrains must reflect a steady-state deformation fabric and should not be influenced by postkinematic annealing (Twiss and Moores, 1992, p. 412).

The first prerequisite is large fulfilled. The second prerequisite, however, is only partly fulfilled because of strain hardening, particularly at advanced state of strain. Further problems are the influence of the stiff anhydrite layer and the rotation of some of the subgrains resulting in new grains.

Away from the anhydrite layer, the subgrain size varies from grain to grain (50–130 µm, Table 1). This range in subgrain size results in a differential stress ranging from 1.6 to 3.8 MPa (Fig. 13). The subgrain size increases significantly adjacent to the rigid anhydrite layer. Here the size is 20–60 µm (Table 1). The corresponding differential stresses are ranging from 3.0 to 8.9 MPa.

4. Discussion

4.1. Microfabrics, deformation mechanisms and flow stress

The microfabrics of the starting samples of Gorleben anhydrite are almost free from deformation fabrics (Zulauf et al., 2010). For this reason the microfabrics of the experimentally deformed samples should largely result from strain that was imposed by the experiments. The macro- and microfabrics observed in the experimentally deformed anhydrite reflect the brittle-viscous transition and are fully consistent with those described for the brittle-viscous regime in the literature (Müller et al., 1981; Ross et al., 1987). The irregularly shaped fracture planes of the experimentally deformed anhydrite boudins are probably related to the heterogeneous composition of the anhydrite concerning grain size and impurities. The macroscopic outline of the anhydrite and evidence for cataclasis in thin sections suggest fracturing to be the main deformation mechanism. Minor crystal plastic deformation is portrayed by twins, undulatory extinction, and serrated twin and grain boundaries. The latter suggest that strain-induced grain-boundary migration had started to be active as a thermally activated deformation process.

Evidence for dislocation creep of the starting samples of Asse halite is indicated by the presence of subgrains (Carter et al., 1982; Urai et al., 1987; Zulauf et al., 2010). Moreover, fluid inclusions, which are present on at least 80% of the grain boundaries, suggest
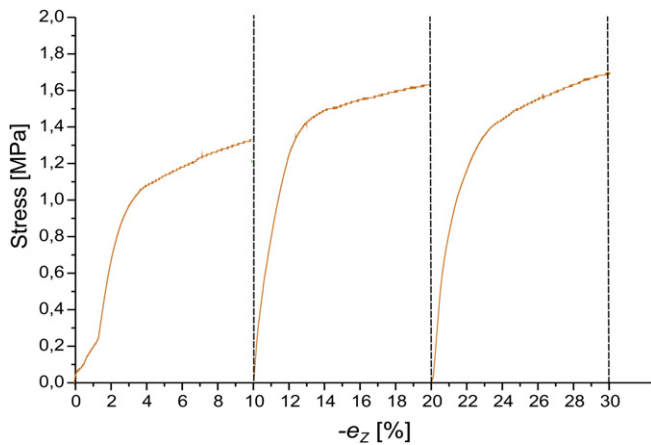
Fig. 7. Stress vs. strain diagram of incremental run with initial layer thickness, $H_i = 2$ mm. $T = 345$ °C; incremental strain, $e_Z = -10\%$; maximum strain, $e_Z = -30\%$; strain rate, $\dot{e} = 1 \times 10^{-7}$ s^{-1}.

that dissolution-reprecipitation creep has also played a role during natural deformation (Urai et al., 1987, see also Schenk and Urai, 2004). The Asse samples used for the present study, however, are largely free from a grain-shape fabric and do not show significant crystal plastic strain. As the strain imposed by the experiments is significant ($e_Z = -40\%$), the weak initial fabrics can be neglected.

Viscous flow of halite during bulk pure flattening is indicated by the oblate grain-shape fabric and by the invasion of viscous halite into the necks between the competent anhydrite boudins. Serrated grain boundaries suggest that grain-boundary migration was active.

EBSD analyses of the experimentally deformed halite revealed a distinct 001-maximum (001-fibre texture) parallel to the Z-axis (Fig. 14b). A similar texture was found in Asse halite deformed experimentally under the same conditions but in a constrictional type of bulk deformation (Zulauf et al., 2010). In the constrictionally deformed samples the 001-maximum, however, is parallel to the X-axis. The observed sets of tightly spaced dark lines, oriented at right angles in sections cut parallel to the Z-axis reflect the {110} planes. As both the Z-axis and the 100-direction bisect the dark lines, the latter should result from slip on {110}<110> (planes hatched in blue in Fig. 14b). Slip along this system also explains the chessboard like subgrain patterns. Since homogeneous crystal plastic strain requires the coeval activity of five independent slip systems, additional slip on {100}<110> should also have been active during the experimental runs (Skrotzki and Welch, 1983). The EBSD analyses and the pole figures also revealed that subgrain rotation was an important recrystallization process resulting in new high-angle grain boundaries and related new recrystallized halite grains.

The differential stress obtained from the size of newly formed subgrains situated remote from the anhydrite layer and remote from primary anhydrite inclusions is largely consistent with the actual stress recorded by the load cell of the machine, although not all of the prerequisites for piezometry are met. The higher differential stress from subgrains situated at the direct contact to anhydrite reflects stress concentration due to the viscosity contrast between both minerals. The load cell is placed on halite monitoring the stress in the direction perpendicular to the layer and parallel to the shortening direction, Z. For this reason the impact of the anhydrite layer on the monitored stress is probably not significant. The stress-strain curves of each experiment should largely reflect the mechanical behavior and the viscosity of the rock-salt matrix. The different flow curves in the stress vs. strain plots may result from slightly different samples of Asse halite. All samples show
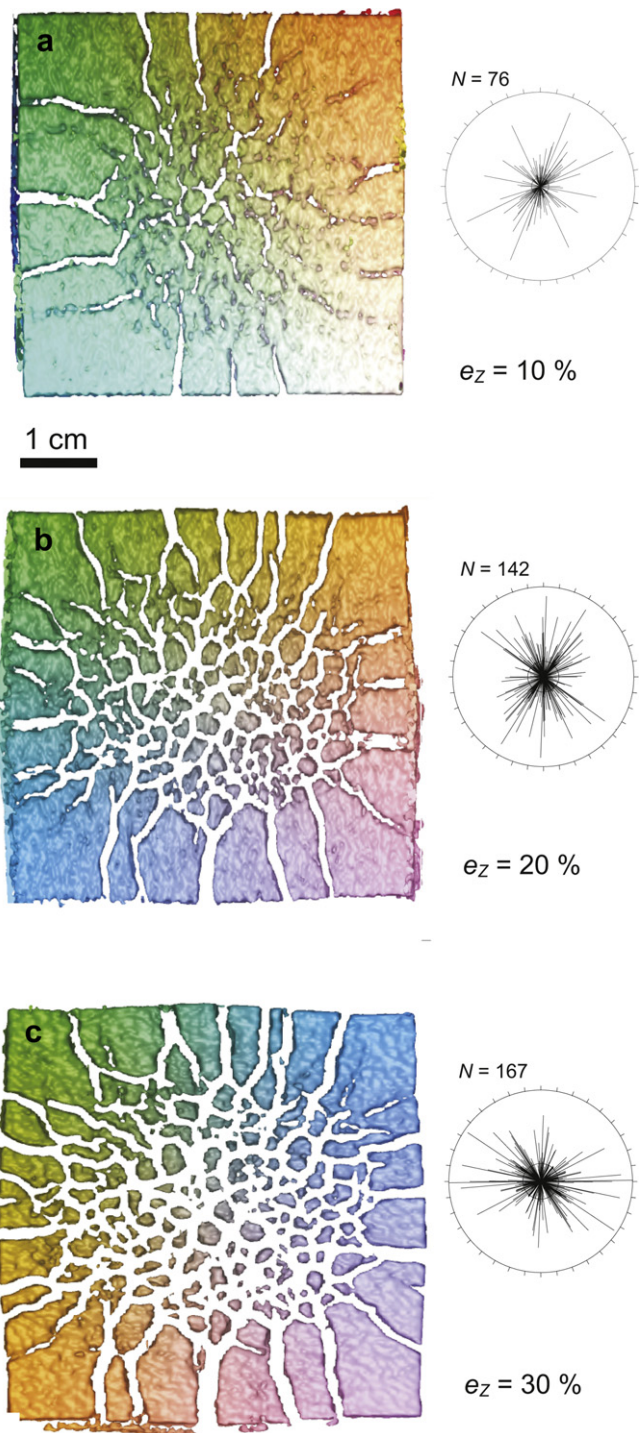

Fig. 8. Computertomographic (CT) images (plan-view) of deformed plasticine layer showing the impact of finite strain on the geometry and number of boudins. View is perpendicular to the layer and parallel to the main shortening direction, Z, respectively. Incremental strain, e_Z, is 10% (a), 20% (b), and 30% (c). Rose diagrams show the distribution of necks in the deformed sample. N is number of measurements.

strain hardening at advanced state of finite strain which is still an open question. Weak to moderate strain hardening, however, does not have a significant impact on the piezometric data (see also Zulauf et al., 2010).

The presence of pervasive subgrains and of newly formed recrystallized grains in the experimentally deformed samples suggests that dislocation creep processes have controlled the
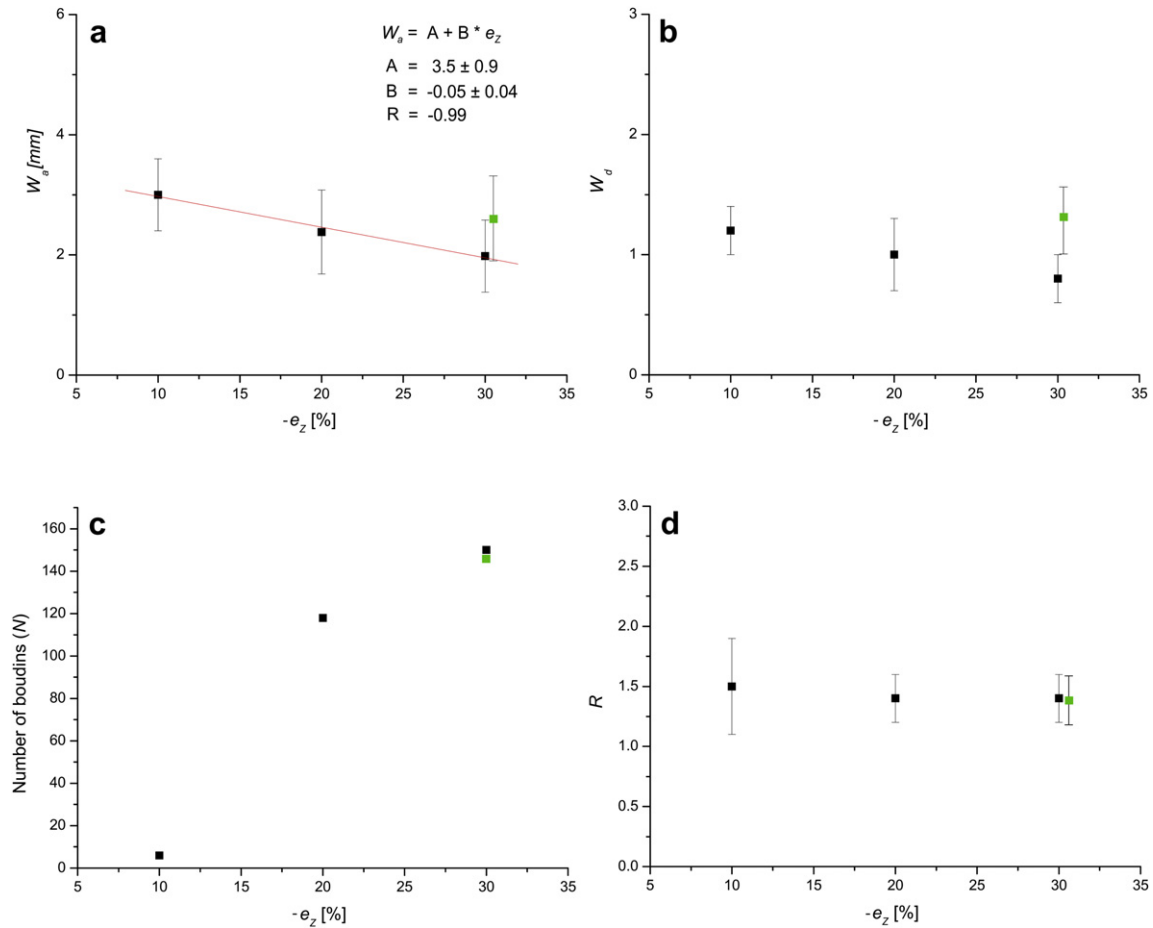
Fig. 9. Geometric data of competent anhydrite layer embedded in viscous matrix of rock salt deformed incrementally under bulk pure flattening conditions with the layer perpendicular to Z. Geometric parameters are plotted vs. finite strain, e_Z. Green filled square describes the data for the case of noninterrupted deformation with initial layer thickness, $H_i = 2.0$ mm. N = number of boudins, R = ratio between long and short axis of boudin in plan-view; W_a = mean diameter of boudins in plan-views, $W_d = W_a/H_f$ = aspect ratio of boudins. Deformation temperature, $T = 345$ °C; incremental strain, e_Z, is 10%; maximum strain, $e_Z = -30\%$; strain rate, $\dot{e} = 1 \times 10^{-7}$ s^{-1}. Data shown have been obtained by Computer Tomography (CT) and by analysis of common sections cut parallel to Z and perpendicular to the layer. (For interpretation of the references to colour in this figure legend, the reader is referred to the web version of this article.)

viscous deformation of Asse halite. In the present case of low stresses ($\sigma < 5$ MPa) steady-state flow can be approximated by the following equation (Carter et al., 1993):

$$\dot{e}' = A\exp\left(-Q/RT10^{-3}\right)\sigma'^{n} \qquad (5)$$

where the pre-exponential constant $A = 8.1 \times 10^{-5}$ MPa^{-n} s^{-1}, the stress exponent $n = 3.4$, the apparent activation energy $Q = 51.6$ J mol^{-1}, the Boltzmann's gas constant, R, is expressed in J mol^{-1} K^{-1}, the temperature, T, is in K, the strain rate, $\dot{e}'$, is in s^{-1}, and the differential stress, σ', is in MPa. The strain rate, $\dot{e}'$, obtained by inserting the piezometrically derived stresses, σ', into Equation (5) are listed in Table 1 and are depicted in Fig. 15. All values show a large uncertainty. When comparing the calculated strain rates, $\dot{e}'$, with the actual (applied) strain rates, $\dot{e}$, it is obvious that the average value of $\dot{e}'$ is close to the strain rate applied during the individual runs if the subgrains used for piezometry are located remote from anhydrite (Fig. 15). In cases where the subgrains are close to anhydrite, the strain rate adjusted is significantly lower than the strain rates based on piezometrically derived stresses. Thus, Equation (5) and the flow parameters obtained by Carter et al. (1993) for a temperature range of 50–200 °C can also be used to describe viscous flow of Asse halite in a flattening type of bulk deformation at $T = 345$ °C and $\dot{e} = 10^{-7}$ s^{-1}.

4.2. Geometry of necks and boudins

The experimental results presented above suggest that boudinage of a competent anhydrite layer inside an incompetent rock-salt matrix in a flattening type of bulk deformation results in irregularly shaped polygonal boudins when the anhydrite layer is oriented perpendicular to the principal shortening axis, Z. These boudins, referred to as 'tablet boudins', are separated by a network of necks, which show either a lack of or a weak preferred orientation in plan-view. The same type of boudin, with similar shape and similar patterns of necks, has been produced experimentally by Ghosh (1988). These experiments, however, were not scaled and the matrix on both sides of the layer was different. Moreover, Ghosh (1988) did not consider different layer thicknesses and did not present quantitative data concerning boudin geometry and rheological parameters of the material used. Tablet-shaped boudins have further been produced using scaled power-law viscous plasticine models as rock analogue (Zulauf et al., 2011a). The geometry of these tablet boudins will be compared with the geometric data of the present study.

The microfabrics of anhydrite suggest that the tablet boudins largely result from brittle tensile failure and thus can be described as torn boudins (sensu Goscombe et al., 2003). The mean diameter of these boudins in plan-views, W_a, is almost the same as the layer
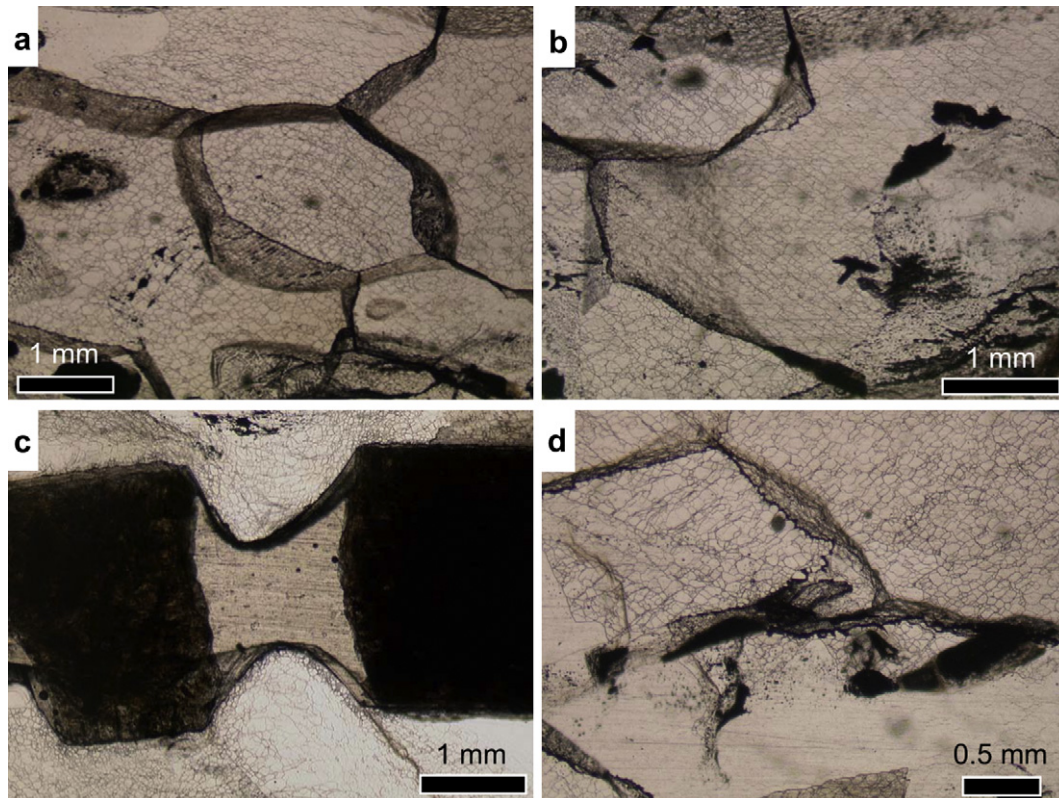
Fig. 10. Microphotographs of deformed halite and anhydrite. (a) Large primary halite grains show dark boundaries which are decorated by numerous fluid inclusions. The discrete dark lines inside the primary grains are boundaries of subgrains which partly rotated forming new recrystallized grains. Note that the number of these subgrains and recrystallized grains is different inside the primary grains. Dark patch inside the grain on the left-hand side is inclusion of primary anhydrite. Parallel polarizers and transmitted light of etched thick section. (b) Subgrain boundaries of halite (discrete dark lines) which are orthogonal to each other resulting in a chessboard pattern inside the large primary grains. The orthogonal subgrain boundaries reflect 110 slip planes. Parallel polarizers and transmitted light of etched thick section (c) Viscous halite is flowing into the neck between anhydrite boudins (dark). The neck is not completely filled with halite. Note the small size of subgrains in halite (discrete dark lines) at the contact to anhydrite and at the margin to the open neck space. Parallel polarizers and transmitted light of etched thick section. (d) Serrated grain boundaries result from interaction of newly formed subgrains with primary grain boundaries. The dark outline of the serrated grain boundaries results from fluid inclusions which include organic matter. Parallel polarizers and transmitted light of etched thick section.

thickness (H_f) resulting in an aspect ratio (W_d) close to 1. This observation is in strong contrast to viscous or viscous-brittle boudinage. The plasticine boudins produced experimentally by Zulauf et al. (2011a) result from an initial phase of viscous necking succeeded by brittle tensile fracture. Their aspect ratio is ranging from ca. 4 to ca. 11, whereas the aspect ratio of the present anhydrite boudins is ranging from 0.8 to 1.5. The latter values are also much lower than the aspect ratios described from boudins in the literature. The aspect ratio of natural torn boudins, which result from extension fractures, is frequently ≥ ca. 1.8 (Price and Cosgrove, 1990; Ghosh and Sengupta, 1999; Van Baelen and Sintubin, 2008), and the averaged aspect ratio is 2.9 (Goscombe et al., 2003). The averaged aspect ratio for necked drawn boudins is 2.6, and for tapering drawn boudins is 4.1 (Goscombe et al., 2003). The aspect ratio of chocolate tablet boudins, exposed in a quartzite/shale sequence along the southwestern coast of Portugal is ca. 3 (Zulauf et al., 2011b). The chocolate-tablet boudins, however, are rectangular in plan-view and result from two-phase deformation, where both phases include an initial phase of viscous necking followed by brittle tensile fracture. Aspect ratios which are close to the values of the present anhydrite boudins have been calculated from experimental anhydrite boudins that developed by tensile fracture in a viscous matrix of rock salt under bulk plane strain and under bulk constriction. In these cases the aspect ratio of the anhydrite boudins is 1.3 ± 0.8 and 1.5 ± 1.0, respectively (Mertineit, 2009; Zulauf et al., 2009). Thus, from the observations and published

data listed above it can be concluded that tensile fracture boudinage results in a much lower boudin aspect ratio than viscous boudinage by formation of pinch-and-swell structures. The difference in geometrical parameters of brittle anhydrite and viscous or brittle-viscous boudins is also documented by the fact that both the number of boudins and the size (mean diameter in plan-views) of boudins show a linear relation with the layer thickness in cases of brittle fracture boudins, but a non-linear relation in cases of viscous or brittle-viscous boudins (Zulauf et al., 2011a). A linear relationship between fracture spacing and layer thickness has also been found in thin competent sedimentary layers (Narr and Suppe, 1991; Van Noten and Sintubin, 2010).

Apart from the aspect ratio, there is also a weak impact of the necking mechanism on the mean diameter, R, of the plasticine boudins in plan-view. The anhydrite boudins, produced in the present study show R-values ranging from 1.2 to 1.9, whereas the plasticine models produced in a flattening type of bulk deformation show values ranging from 1.2 to 2.6 (Zulauf et al., 2011a).

To check the impact of the interruption phase of the incremental studies, we carried out one additional run with the same type of sample and the same boundary conditions, but without interruption (see green symbols in Fig. 9). It is obvious that the mean boudin diameter, W_a, is higher if the finite strain, $e_Z = 30\%$, was attained without break. The smaller size of the incrementally produced boudins can be explained by the strong temperature change due to deformation break. Cooling to room temperature and subsequent

Table 1
Deformation parameters of thermomechanical runs and piezometric data. Differential stress, σ', was obtained from subgrain size, D, using the following equation: σ' (MPa) = $107D^{-0.87}$ (μm). Strain rate, $\dot{e}'$, based on piezometric data, was calculated using Equation (5).

		at contact to anhydrite		remote from contact				
		grain 0/1 adjacent to anhydrite, direct contact	grain 0/2 adjacent to anhydrite, no direct contact	grain 1 remote from anhydrite	grain 2 remote from anhydrite	grain 3 remote from anhydrite	grain 4 remote from anhydrite	grain 5 remote from anhydrite
mean subgrain size, D	mm	0.028	0.044	0.069	0.089	0.083	0.088	0.088
2σ subgrain size	mm	0.011	0.017	0.022	0.040	0.027	0.035	0.033
stress (max.)	MPa	8.88	6.11	3.80	3.57	3.22	3.36	3.31
stress (mean)	MPa	5.83	4.00	2.70	2.15	2.29	2.17	2.19
stress (min.)	MPa	4.40	3.01	2.11	1.56	1.79	1.63	1.65
strainrate (max)	[s^{-1}]	5.9E-06	1.7E-06	3.3E-07	2.7E-07	1.9E-07	2.2E-07	2.1E-07
strainrate (mean)	[s^{-1}]	1.4E-06	3.9E-07	1.0E-07	4.8E-08	5.9E-08	4.9E-08	5.0E-08
strainrate (min)	[s^{-1}]	5.4E-07	1.5E-07	4.5E-08	1.6E-08	2.6E-08	1.9E-08	1.9E-08

heating to deformation temperature (T = 345 °C) might have produced additional tensile fractures in the anhydrite layer due to different thermal expansion of rock salt and anhydrite. Such a strong impact of deformation breaks has not been observed when using plasticine as rock analogue (Zulauf and Zulauf, 2005; Zulauf et al., 2011a).

A further problem concerns the effects of the layer thickness on the quality of geometric data obtained in the performed experiments. The scatter of geometric data and the uncertainties of geometrical parameters are highest if the layer is very thin (1 mm). This feature has also been observed in the plasticine models (Zulauf et al., 2011a) and is probably related to the fact that the impact of primary instabilities inside the anhydrite layer, such as impurities or variation in grain size, on the deformation structure is much stronger in thinner than in thicker layers. Moreover, the resolution of the medical computer tomography is at its limit concerning the resolution if the thickness of the anhydrite layer is only 1 mm. Layers which are smaller than 1 mm require a micro-computertomograph in order to obtain robust 3D geometric data.

4.3. Theory for fracture spacing and boudinage of the competent layer under bulk pure flattening

In contrast to the plasticine models and natural boudins mentioned above, the competent anhydrite layer of the present study did not undergo significant viscous necking before tensile failure led to the formation of boudins. Boudinage of anhydrite by formation of extension (opening-mode) fractures should be controlled by the transfer of stress from the viscous matrix of rock salt to the brittle anhydrite layer (Ramberg, 1955; Lloyd et al., 1982). Boudinage develops by successive 'mid-point' fracturing of the layer segments, until the anhydrite layer is reduced to boudins, all of which are shorter than some critical length, i.e. the length for which the tensile fracture strength of the anhydrite layer is higher than the tensile stress at the mid-point (Ramberg, 1955). The Ramberg model is consistent with the results of experiments and numerical modeling, which show that with increasing applied layer-parallel strain, fracture spacing decreases approximately as the inverse of the applied strain by sequential infilling of opening-mode fractures between existing fractures up to a critical fracture spacing to layer thickness (aspect) ratio (e.g. Garret and Bailey, 1977; Manders et al., 1983; Wu and Pollard, 1995). If this ratio is attained, tensile stresses inside the existing boudins are too low for the production of new fractures and the additional strain is accommodated by opening of the existing fractures resulting in necks. In this particular case, the spacing scales with layer thickness, which is referred to as fracture saturation (Aveston et al., 1971; Cobbold, 1979; Bai et al., 2000). The concept of fracture

saturation is based on frictional coupling between the competent layer (boudins) and the incompetent matrix. The modeling results of Bai et al. (2000) and Bai and Pollard (2000b) indicate that fracture saturation results from a domain of compressive layer-parallel
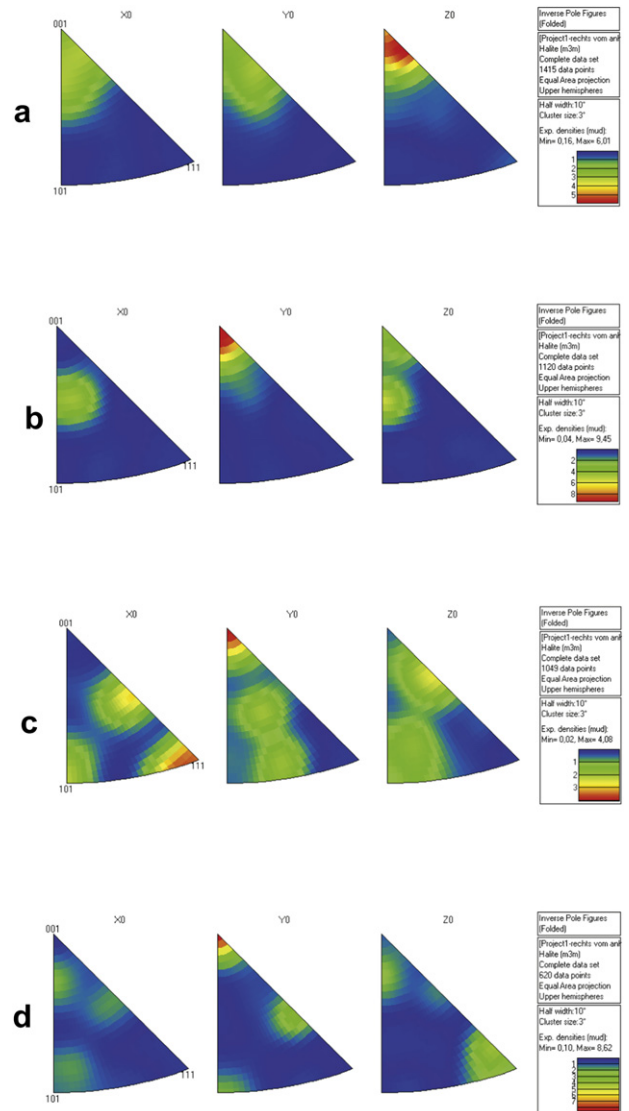

Fig. 11. Inverse pole figures of experimentally deformed halite matrix based on EBSD analyses. Equal-area upper-hemisphere projection.
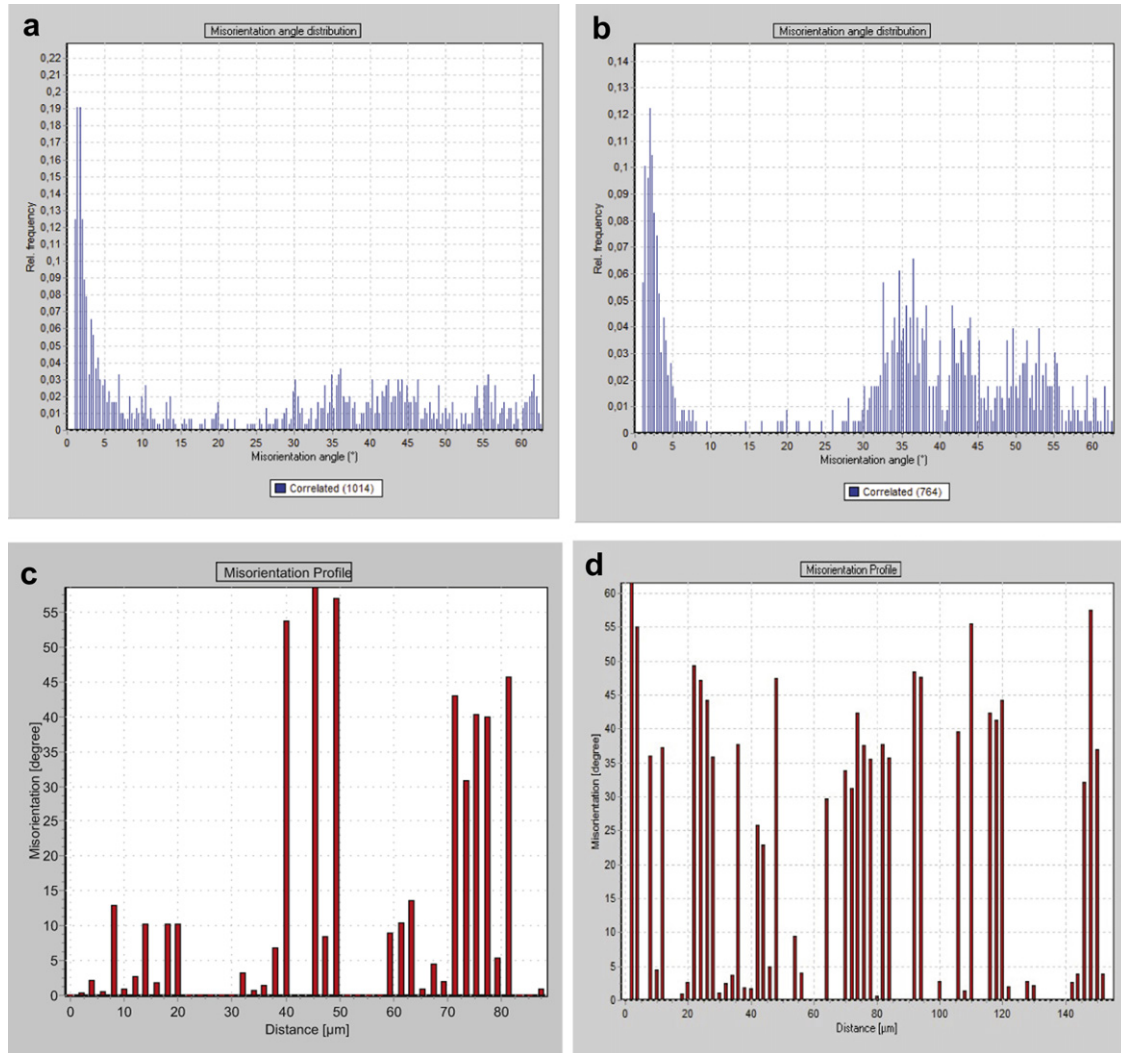
Fig. 12. Frequency and spatial distribution of misorientation data obtained from two different deformed halite grains, situated close to the anhydrite boudin (a, c), and remote from the anhydrite boudin (b, d).
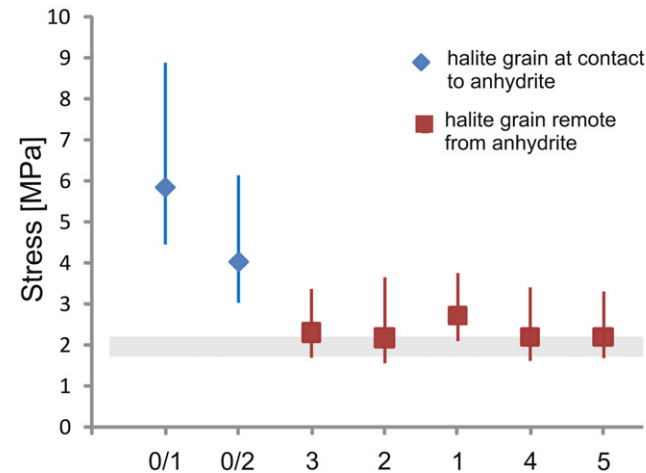

Fig. 13. Differential stress obtained using the subgrain size of halite of deformed sample with H_i of anhydrite layer is 2.5 mm. Horizontal grey bar shows the peak stress recorded by the load cell of the machine. Sample numbers are listed along the horizontal axis.

stress that is attained at an aspect ratio of ca. 1. As this value is compatible with the aspect ratio of the anhydrite boudins of the present study, interfacial slip between anhydrite and rock salt was probably not significant. In a layered system where interfacial slip is possible, fracture spacing is not an indicator for fracture saturation, because interfacial slip results in increase of the fracture spacing (Schöpfer et al., 2011). Increased fracture spacing might further be supported by elevated pore pressure (e.g. Secor, 1965) or by pre-existing flaws in the competent layer (Bai and Pollard, 2000a). A reduction of fracture spacing, on the other hand, might be caused by an increase in lithostatic pressure/and or a decrease of pore pressure, which causes stronger frictional coupling between layer and matrix.

All of the models and theories discussed above are based on plane strain, whereas the present experiments were carried out under bulk pure flattening. This difference might be significant when comparing the results of the present study with existing models (Fletcher, 1995). As the strain rate of the competent anhydrite layer and the incompetent rock-salt matrix is different, the axisymmetric stress configuration, with the main principal stress, σ_1, parallel to the principal shortening direction, Z, is causing shear stress along the layer/matrix interface, which has a radial attitude and results in tensile stress and boudinage of the anhydrite layer.
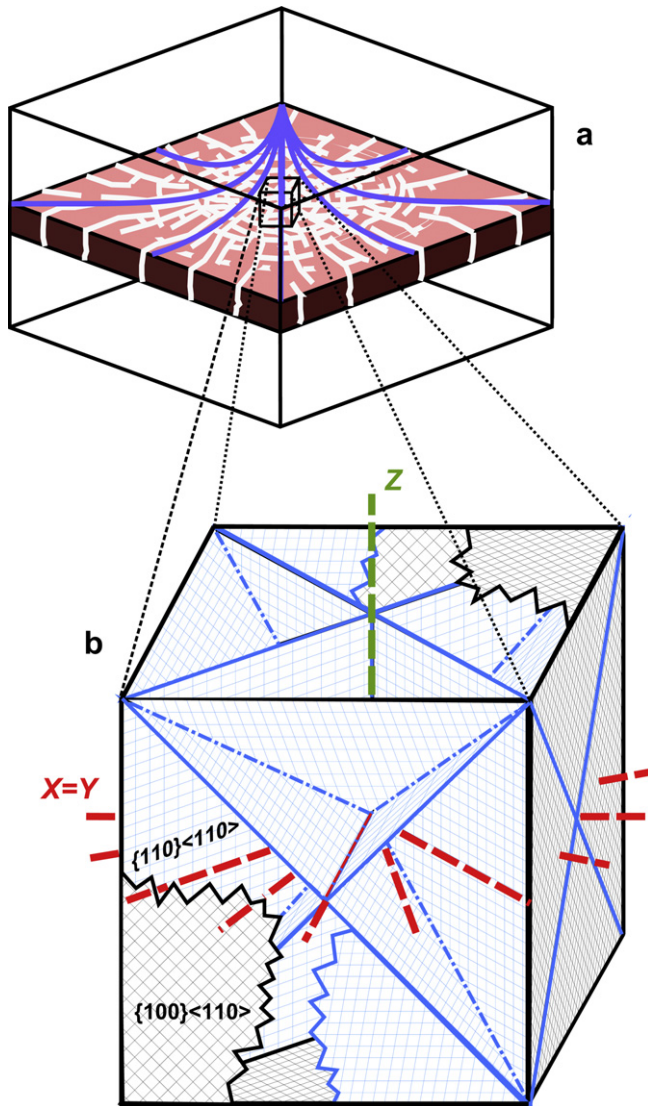
Fig. 14. Relation between structure and texture in halite of deformed models. (a) Schematic model of the development of noncylindrical boudins under bulk pure flattening with the layer perpendicular to the main shortening direction, *Z*. White lines show the distribution of concentric and radial necks in the anhydrite layer (idealized). Blue lines show the particle paths in the rock-salt matrix. (b) Slip systems in halite and distribution of the principal strain axes (*X, Y, Z*) in a flattening type of bulk deformation. (For interpretation of the references to colour in this figure legend, the reader is referred to the web version of this article.)

Because of the limited dimension of the models, the tensile stress in the anhydrite layer decreases radially from the center of the sample towards its margins (Fig. 14a). This is the reason why the intensity of boudinage decreases towards the margins of the models. All of the models run in the experiments show this strong boundary effect which had to be considered when carrying out the statistical analysis of geometrical parameters.

The reasons why the shape of the boudins is not entirely isometric and why the orientation of the necks is not perfectly random are not fully understood. It might be possible that the non-isometric shape is supported by primary instabilities in the anhydrite and rock salt which are causing mechanical anisotropies. Another reason, which is probably more significant for the non-isometric shape than material impurities, could be related to the mechanism by which tensile fractures are growing in space and time (Zulauf et al., 2011a). The radial shear stress along the layer/
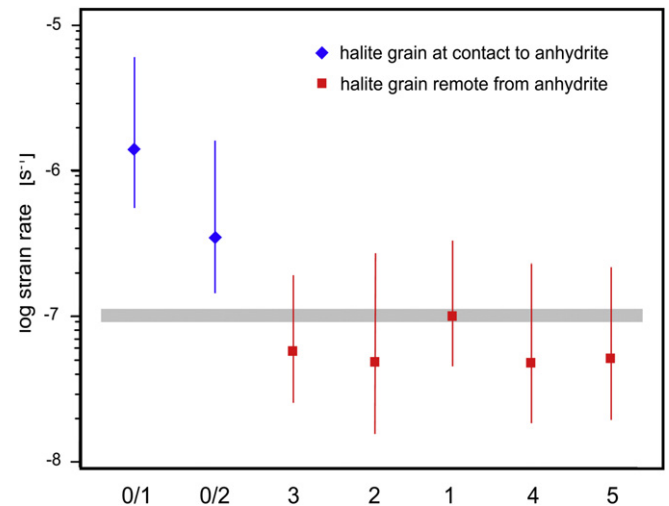

Fig. 15. Plot showing experimental strain rate (horizontal gray bar) compared with strain rates that were calculated using Equation (5) and stress values derived from subgrain size of halite (sample number is indicated along the horizontal axis). For further explanation, see text.

matrix interface results in tensile stress inside the layer that will produce failure as soon as its tensile strength is exceeded. This failure results in tension fractures which have a concentric geometry in plan-view (Fig. 14a). This permanent stretch of the layer in radial direction is inevitably associated with a stretch in concentric direction. If the latter reaches a critical value, the layer will be affected by a second set of fractures, which have a radial orientation in plan-view. In praxis both fracture systems (concentric and radial) should form almost simultaneously, meaning that the presence of one fracture type is affecting the growth and orientation of the other type and vice versa (Zulauf et al., 2011a). The strong interaction of both fracture systems implies that concentric and radial tension fractures are hardly developed, and a regular network of fractures cannot form in a flattening type of bulk deformation.

4.4. Natural examples of brittle tablet boudins

The radial and concentric necks, which are particularly well developed in the case where the thickness of the anhydrite layer, $H_i = 1.5$ mm (Fig. 5c), are similar to those of salt glaciers of Qum Kuh, Iran, which result from extrusion of salt and outward radial flow away and downslope from the extrusive orifice (Talbot and Aftabi, 2004).

Natural examples of noncylindrical boudins, and tablet boudins in particular, are rare. Concerning salt rocks, noncylindrical boudinage has been described by Siemeister (1969, Fig. 2 of Table 6), who found irregularly distributed boudins of competent rock salt inside an incompetent carnallite matrix. As bulk flattening is common in nature (Pfiffner and Ramsay, 1982), the number of natural tablet boudins is probably higher than assumed. As tablet bouins require exposure in three dimensions or at least plan-views to be identified in the field or in mines, most of them have probably not been recognized.

5. Conclusions

The following conclusions can be drawn from the present study:

- The principal deformation mechanisms of the competent layer and of the incompetent matrix have a significant impact on the geometry of boudins. This holds probably for all types of bulk deformation (flattening, plane, constriction).

- The aspect ratio of tensile fracture boudins is much lower than the aspect ratio of boudins which result from viscous or brittle-viscous necking.
- Number and size of boudins show a linear relation to the layer thickness in cases of tensile fracture boudinage, whereas viscous and brittle viscous models imply a non-linear relation.
- Future studies should focus on similar experiments but using higher deformation temperatures to constrain the geometrical boudin parameters in cases where both halite and anhydrite are deformed by dislocation creep and the competent anhydrite layer is dissected by viscous necking.

Acknowledgements

References

Aveston, J., Cooper, G.A., Kelly, A., 1971. The Properties of Fiber Composites. IPC Sci. Technol. Press.

Bai, T., Pollard, D.D., 1999. Spacing of fractures in a multilayer at fracture saturation. Int. J. Fracture 100, L23–L28.

Bai, T., Pollard, D.D., 2000a. Closely spaced fractures in layered rocks: initiation mechanism and propagation kinematics. J. Struct. Geol. 22, 1409–1425.

Bai, T., Pollard, D.D., 2000b. Fracture spacing in layered rocks: a new explanation based on the stress transition. J. Struct. Geol. 22, 43–57.

Bai, T., Pollard, D.D., Gao, H., 2000. Explanation for fracture spacing in layered materials. Nature 403, 753–756.

Bäuerle, G., 1998. Sedimentäre Texturen und Stylolithen am Top des Hauptanhydrits (Zechstein 3) im Salzstock Gorleben. Diploma thesis, Hannover University, Hannover, 97p. (unpublished).

Bestmann, M., Piazolo, S., Spiers, C.J., Prior, D.J., Franssen, R.C.M.W., 2005. Microstructural evolution during initial stages of static recovery and recrystallization: new insights from in-situ heating experiments combined with electron backscatter diffraction analysis. J. Struct. Geol. 27, 447–457.

Borchert, H., Muir, R.O., 1964. Salt Deposits. The Origin, Metamorphism and Deformation of Evaporites. D. van Nostrand Company, Ltd, London. 338 p.

Bornemann, O., Behlau, J., Fischbeck, R., Hammer, J., Jaritz, W., Keller, S., Mingerzahn, G., Schramm, M., 2008. Standortbeschreibung Gorleben, Teil 3: Ergebnisse der über- und untertägigen Erkundung des Salinars. Geologisches Jahrbuch C73, 5–211. Hannover.

Carter, N.L., Hansen, F.D., Senseny, P.E., 1982. Stress magnitudes in natural rock salt. J. Geophys. Res. 87, 9289–9300.

Carter, N.L., Horseman, S.T., Russell, J.E., Handin, J., 1993. Rheology of rocksalt. J. Struct. Geol. 15, 1257–1271.

Cobbold, P.R., 1979. Origin of periodicity: saturation or propagation? J. Struct. Geol. 1, 96.

Fletcher, R.C., 1995. Three-dimensional folding and necking of a power-law layer: are folds cylindrical, and, if so, do we understand why? Tectonophysics 247, 65–83.

Franssen, R.C.M.W., 1993. Rheology of synthetic rock salt with emphasis on the influence of deformation history and geometry on the flow behavior. PhD thesis, Rijksuniversiteit Utrecht.

Franssen, R.C.M.W., 1994. The rheology of synthetic rocksalt in uniaxial compression. Tectonophysics 233, 1–40.

Gairola, V.K., Kern, H., 1984. Microstructure and texture in experimentally folded single-layer rock salt. J. Struct. Geol. 6, 201–213.

Garret, K.W., Bailey, J.E., 1977. Multiple transverse fracture in 90° cross-ply laminates of a glass fibre-reinforced polyester. J. Mater. Sci. 12, 157–168.

Ghosh, S.K., 1988. Theory of chocolate tablet boudinage. J. Struct. Geol. 10, 541–553.

Ghosh, S.K., Sengupta, S., 1999. Boudinage and composite boudinage in superposed deformations an syntectonic migmatization. J. Struct. Geol. 21, 97–110.

Goscombe, B.D., Passchier, C.W., Hand, M., 2003. Boudinage classification: end-member boudin types and modified boudin structures. J. Struct. Geol. 26, 739–763.

Guillopé, M., Poirier, J.P., 1979. Dynamic recrystallization during creep of single-crystalline halite: an experimental study. J. Geophys. Res. 84, 5557–5567.

Hubbert, M.K., 1937. Theory of scale models as applied to the study of geologic structures. Geol. Soc. America Bull. 48, 1459–1519.

Hudec, M.R., Jackson, M.P.A., 2007. Terra infirma: understanding salt tectonics. Earth-Science Rev. 82, 1–28.

Jackson, M.P.A., Talbot, C.J., 1986. External shapes, strain rates, and dynamics of salt structures. Bull. Geol. Soc. Am. 97, 305–323.

Jackson, M.P.A., 1995. Retrospective salt tectonics. In: Jackson, M.P.A., Roberts, D.G., Snelson, S. (Eds.), Salt Tectonics: A Global Perspective, vol. 65. AAPG Memoir, pp. 1–28.

Jackson, M.P.A., Talbot, C.J., 1987. Anatomy of mushroom shaped diapirs. J. Struct. Geol. 11, 211–230.

Lloyd, G.E., Ferguson, C.C., Reading, K., 1982. A stress-transfer model for the development of extension fracture boudinage. J. Struct. Geol. 4, 355–372.

Manders, P.T., Chou, T.-S., Jones, F.R., Rock, J.W., 1983. Statistical analysis of multiple fracture in 00°/90° glass fibre/epoxy resin laminates. J. Mater. Sci. 18, 2876–2889.

Mertineit, M., 2009. Faltung und Boudinage einer Anhydritlage in Halitmatrix unter ebenen Verformungsbedingungen: Ergebnisse thermomechanischer Experimente. Diploma thesis, Goethe University, Frankfurt a.M., 77 p. (unpublished).

Müller, W.H., Schmid, S.M., Briegel, U., 1981. Deformation experiments on anhydrite rocks of different grain sizes: rheology and microfabric. Tectonophysics 78, 527–543.

Narr, W., Suppe, J., 1991. Joint spacing in sedimentary rocks. J. Struct. Geol. 13, 1037–1048.

Pennock, G.M., Drury, M.R., Spiers, C.J., 2005. The development of subgrain misorientations with strain in dry synthetic NaCl measured using EBSD. J. Struct. Geol. 27, 2159–2170.

Pfiffner, O.A., Ramsay, J.G., 1982. Constraints on geological strain rates: arguments from finite strain states of naturally deformed rocks. J. Geophys. Res. 87, 311–321.

Price, N.J., Cosgrove, J.W., 1990. Analysis of Geological Structures. Cambridge University Press, Cambridge.

Ramberg, H., 1955. Natural and experimental boudinage and pinch-and-swell structures. J. Geol. 63, 512–526.

Ramberg, H., 1981. Gravity, Deformation and the Earth's Crust. Academic Press, London. 452p.

Reber, J.E., Schmalholz, S.M., Burg, J.-P., 2010. Stress orientation and fracturing during three-dimensional buckling: numerical simulation and application to chocolate-tablet structures in folded turbidites, SW Portugal. Tectonophysics 493, 187–195.

Ross, J.V., Bauer, S.J., Hansen, F.D., 1987. Textural evolution of synthetic anhydrite-halite mylonites. Tectonophysics 140, 307–326.

Schenk, O., Urai, J.L., 2004. Microstructual evolution and grain boundary structure during static recrystallization in synthetic polycrystals of sodium chloride containing saturated brine. Contrib. Mineral. Petrol. 146, 671–682.

Schléder, Z., Urai, J.L., 2005. Microstructural evolution of deformation-modified primary halite from the Middle Triassic Röt Formation at Hengelo, The Netherlands. Int. J. Earth Sci. 94, 941–955.

Schléder, Z., Urai, J.L., 2007. Deformation and recrystallization mechanisms in mylonitic shear zones in naturally deformed extrusive EoceneOligocene rocksalt from Eyvanekey plateau and Garmsar hills (central Iran). J. Struct. Geol. 29, 241–255.

Schoenherr, J., Urai, J.L., Kukla, P.A., Littke, R, Schleder, Z., Larroque, J.-M., Newall, M., 2007. Salt: a case study of the infra-Cambrian Ara salt from the South Oman salt Basin. AAPG Bull. 91, 1541–1557.

Schöpfer, M.P.J., Arslan, A., Walsh, J.J., Childs, C., 2011. Reconciliation of contrasting theories for fracture spacing in layered rocks. J. Struct. Geol. 33, 551–565.

Secor, D.T., 1965. Role of fluid pressure in jointing. Am. J. Sci. 263, 633–646.

Siemeister, G., 1969. Primärparagenese und Metamorphose des Ronneberglagers nach Untersuchungen im Grubenfeld Salzdetfurth. Beihefte Zum Geologischen Jahrbuch 62, 1–22. Hannover.

Skrotzki, W., Welch, P., 1983. Development of texture and microstructure in extruded ionic polycrystalline aggregates. Tectonophysics 99, 47–61.

Spiers, C.J., Schutjens, P.M.T.M., Brzesowsky, R.H., Peach, C.J., Liezenberg, J.L., Zwart, H.J., 1990. Experimental determination of constitutive parameters governing creep of rocksalt by pressure solution. In: Knipe, R.J., Rutter, E.H. (Eds.), Deformation Mechanisms, Rheology, and Tectonics. Geol. Soc. London, Special Publ., vol. 54, pp. 215–227.

Talbot, C.J., Aftabi, P., 2004. Geology and models of salt extrusion at Qum Kuh, Central Iran. Journal of the Geological Society, London 161, 321–334.

Talbot, C.J., Tully, C.P., Woods, P.J.E., 1982. The structural geology of Boulby (potash) mine, Cleveland, United Kingdom. Tectonophysics 85, 167–204.

Ter Heege, J.H., De Bresser, J.H.P., Spiers, C.J., 2005. Rheological behavior of synthetic rocksalt: the interplay between water, dynamic recrystallization and deformation mechanisms. J. Struct. Geol. 27, 948–963.

Twiss, R.J., 1977. Theory and applicability of a recrystallized grain size paleopiezometer. Pure Appl. Geophys 115, 225–244.

Twiss, R.J., Moores, E.M., 1992. Structural Geology. W.H. Freeman & Co, New York, 532 p.

Urai, J.L., Spiers, C.J., Peach, C.J., Franssen, R.C.M.W., Liezenberg, J.L., 1987. Deformation mechanisms operating in naturally deformed halite rocks as deduced from microstructural investigations. Geol. Mijnbouw. 66, 165–176.

Urai, J.L., Spiers, C.J., 2007. The effect of grain boundary water on deformation mechanisms and the rheology of rocksalt during long-term deformation. In: Wallner, M., Lux, K.-H., Minkley, W., Hardy Jr., H.R. (Eds.), The Mechanical Behavior of Salt – Understanding of THMC Processes in Salt. Taylor & Francis Group, London, pp. 149–158.

Van Baelen, H., Sintubin, M., 2008. Kinematic consequences of an angular unconformity in simple shear: an example from the southern border of the Lower Palaeozoic Rocroi inlier (Naux, France). Bulletin del la Société géologique de France 179, 73–87.

Van Gent, H., Urai, J.L., de Keijzer, M, 2011. The internal geometry of salt structures. - A first look using 3D seismic data from the Zechstein of the Netherlands. J. Struct. Geol. 32, 537–553.

Van Noten, K., Sintubin, M., 2010. Linear to non-linear relationship between vein spacing and layer thickness in centimeter- to decimeter-scale siliciclastic multilayers from the High-Ardenne slate belt (Belgium, Germany). J. Struct. Geol. 32, 377–391. doi:10.1016/j.jsg.2010.01.011.

Wu, H., Pollard, D.D., 1995. An experimental study of the relationship between joint spacing and layer thickness. J. Struct. Geol. 17, 887–905.

Weijermars, R., 1997. Principles of Rock Mechanics. Alboran Science Publishing. 359 p.

Zulauf, G., Zulauf, J., Hastreiter, P., Tomandl, B., 2003. A deformation apparatus for threedimensional coaxial deformation and its application to rheologically stratified analogue material. Journal of Structural Geology 25, 469–480.

Zulauf, J., Zulauf, G., 2005. Coeval folding and boudinage in four dimensions. J. Struct. Geol. 27, 1061–1068.

Zulauf, G., Gutiérrez-Alonso, G., Kraus, R., Petschick, R., Potel, S, 2011b. Formation of chocolate ablet boudins in a foreland fold and thrust belt: a case study from the external Variscides (Almograve, Portugal). J. Struct. Geol. 33, 1639–1649. doi:10.1016/j.jsg.2011.08.009.

Zulauf, G., Zulauf, J., Bornemann, O., Brenker, F., Höfer, H., Peinl, M., Woodland, A., 2010. Experimental deformation of a single-layeranhydrite in halite matrix under bulk constriction. Part 2: microfabrics and deformation mechanisms. J. Struct. Geol. 32, 264–277. doi:10.1016/j.jsg.2009.12.001.

Zulauf, J., Zulauf, G., Kraus, R., Gutiérrez-Alonso, G., Zanella, F., 2011a. The origin of tablet boudinage: results from experiments using power-lawrock analogs. Tectonophysics 510, 327–336. doi:10.1016/j.tecto.2011.07.013.

Zulauf, G., Zulauf, J., Bornemann, O., Kihm, N., Peinl, M., Zanella, F., 2009. Experimental deformation of a single-layer anhydrite in halite matrix under bulk constriction. Part 1: geometric and kinematic aspects. J. Struct. Geol. 31, 460–474. doi:10.1016/j.jsg.2009.01.013.